

# $\phi$ and $\Omega$ production from relativistic heavy ion collisions in a dynamical quark coalescence model

Lie-Wen Chen<sup>1,2</sup> and Che Ming Ko<sup>3</sup>

<sup>1</sup>*Institute of Theoretical Physics, Shanghai Jiao Tong University, Shanghai 200240, China*

<sup>2</sup>*Center of Theoretical Nuclear Physics, National Laboratory of Heavy Ion Accelerator, Lanzhou 730000, China*

<sup>3</sup>*Cyclotron Institute and Physics Department, Texas A&M University, College Station, Texas 77843-3366*

(Dated: February 9, 2020)

Based on the phase-space information obtained from a multi-phase transport model within the string melting scenario for strange and antistrange quarks, we study the yields and transverse momentum spectra of  $\phi$  mesons and  $\Omega$  ( $\Omega^- + \bar{\Omega}^+$ ) baryons as well as their anisotropic flows in Au+Au collisions at RHIC using a dynamical quark coalescence model that includes the effect due to quark phase-space distributions inside hadrons. With current quark masses and fixing the radii of  $\phi$  mesons and  $\Omega$  baryons from fitting the measured yields, we first study the ratio of the yield of  $\Omega$  baryons to that of  $\phi$  mesons as well as their elliptic and fourth-order flows as functions of the transverse momentum. How the elliptic and fourth-order flows of  $\phi$  mesons and  $\Omega$  baryons are related to those of strange and antistrange quarks is then examined. The dependence of above results on the radii of  $\phi$  mesons and  $\Omega$  baryons as well as on the strange quark mass is also studied.

PACS numbers: 12.38.Mh, 5.75.Ld, 25.75.-q, 24.10.Lx

## I. INTRODUCTION

Recently, there is a lot of interest in using the quark coalescence or recombination model to understand the experimental data from heavy ion collisions at the Relativistic Heavy Ion Collider (RHIC). As shown in Refs. [1, 2, 3, 4], the quark coalescence model can explain successfully the observed anomalously large enhancement of baryon to meson ratio at intermediate transverse momenta and the scaling of the elliptic flow of identified hadrons according to their valence quark numbers. Most of these applications of the quark coalescence model were based on a simple momentum-space coalescence in which only quarks with same momentum can coalesce into hadrons. Also, the phase-space information of quarks in the partonic matter produced in relativistic heavy ion collisions is usually taken from a schematic fireball model. Although the fireball model was still used in Ref. [1], the probabilities for quarks to coalesce into hadrons were calculated using the quark Wigner phase-space function inside hadrons that is based on the constituent quark model. Only in Ref. [5] was the coalescence probability calculated also with a quark phase-space information from a dynamical parton cascade model. Results from such a dynamical quark coalescence model indicate that the phase-space structure of quarks at freeze out plays an important role in hadron production from the quark-gluon plasma. In the present study, we use the dynamical quark coalescence model that is based on the quark phase-space information obtained from a multi-phase transport (AMPT) model within the string melting scenario and the quark Wigner phase-space function inside hadrons from the constituent quark model to study the production of  $\phi$  mesons and  $\Omega$  ( $\Omega^- + \bar{\Omega}^+$ ) baryons and their anisotropic flows in Au+Au collisions at RHIC.

The study of  $\phi$  meson and  $\Omega$  baryon production in relativistic heavy-ion collisions is a topic of great interest as

one of the signatures for the quark-gluon plasma (QGP) produced in relativistic heavy-ion collisions is enhanced production of hadrons consisting of strange and/or antistrange quarks. This is due to the fact that masses of strange quarks are comparable to the temperature of the QGP and are thus expected to be abundantly produced from quark and gluon inelastic scattering once the QGP is formed in the collisions [6, 7]. Since the  $\phi$  meson carries hidden strangeness ( $s\bar{s}$ ) and the  $\Omega$  baryon consists of three valence strange quarks ( $sss$ ) or antistrange quarks ( $\bar{s}\bar{s}\bar{s}$ ), their production in heavy-ion collisions would also be enhanced if the QGP is formed.

Furthermore, anisotropic flows of  $\phi$  mesons and  $\Omega$  baryons in relativistic heavy ion collisions are useful for understanding the collective dynamics of strange quarks in the produced QGP [8, 9]. It has been known that anisotropic flows are sensitive to the properties of dense matter formed during the early stage of heavy ion collisions [10, 11, 12, 13]. This sensitivity not only exists in the elliptic flow  $v_2$  [14, 15, 16, 17, 18, 19, 20, 21] but also in the smaller higher-order anisotropic flows, such as the fourth-order anisotropic flow  $v_4$  [22, 23, 24, 25, 26, 27, 28]. Moreover, observed hadron elliptic flows in heavy-ion collisions at RHIC were found to satisfy the valence quark number scaling, i.e., the elliptic flow per quark is the same at same transverse momentum per quark. As shown in Refs. [1, 2, 3, 4], such a scaling of hadron elliptic flows according to their valence quark numbers can be understood in the quark recombination/coalescence model. Other scaling relations among hadron anisotropic flows, such as  $v_4(p_T) \sim v_2^2(p_T)$ , have also been observed in experimental data [26], and they have been shown in the quark coalescence model to relate to similar scaling relations among quark anisotropic flows [27, 28]. Because of their small scattering cross sections with other hadrons [29, 30, 31, 32, 33, 34, 35],  $\phi$  mesons and  $\Omega$  baryons are not much affected by rescattering effects in later hadronic

stage of the collisions and are thus expected to carry more directly the information on the properties of the QGP and how they are produced during the hadronization [36, 37, 38, 39].

Our study shows that in heavy ion collisions at RHIC the ratio of the yield of  $\Omega$  baryons to that of  $\phi$  mesons at intermediate transverse momenta is strongly enhanced compared to that at low transverse momenta, similar to that observed in the data for the proton to pion ratio. Also, the elliptic flows  $v_2(p_T)$  of  $\phi$  mesons and  $\Omega$  baryons follow approximately the valence quark number scaling. Their valence-quark-number scaled elliptic flows deviate, however, strongly from the elliptic flow of strange and antistrange quarks. For the forth-order anisotropic flow  $v_4(p_T)$ , it scales with the square of the elliptic flow for both  $\phi$  mesons and  $\Omega$  baryons. We have also studied the dependence of above results on the radii of  $\phi$  mesons and  $\Omega$  baryons as well as on the strange quark mass. For physically reasonable radii, both yields of  $\phi$  mesons and  $\Omega$  baryons increase with increasing radii. Their yields eventually decrease as the radii become unrealistically large. The scaled elliptic flows of both  $\phi$  mesons and  $\Omega$  baryons increase with increasing radii and approach that of strange and antistrange quarks for very large radii as in the naive momentum-space quark coalescence model. Changing strange and antistrange quark masses to their constituent quark masses affects significantly the yields of  $\phi$  mesons and  $\Omega$  baryons but not much their anisotropic flows. Our results therefore suggest that both the dynamical phase-space information of partons at freeze out and quark structure of hadrons are important for  $\phi$  meson and  $\Omega$  baryon production in relativistic heavy ion collisions. We note that our study based on a dynamical quark coalescence model for  $\phi$  meson production and elliptic flow in relativistic heavy ion collisions is different from that of Ref. [8], where  $\phi$  mesons were reconstructed from the invariant mass distributions of kaons and antikaons from the AMPT model.

The paper is organized as follows. In Section II, we briefly review the AMPT model and present detailed information on the dynamics of quarks and antiquarks (also called partons) in heavy ion collisions at RHIC. In Section III, the dynamical quark coalescence model based on the parton phase-space distributions at freeze out is described for  $\phi$  meson and  $\Omega$  baryon production. This also includes the construction of the quark Wigner phase-space functions inside  $\phi$  mesons and  $\Omega$  baryons. The dynamical quark coalescence model is then used in Section IV to study the yields and transverse momentum spectra as well as the anisotropic flows of  $\phi$  mesons and  $\Omega$  baryons in Au+Au collisions at RHIC. In Section V, the dependence of above results on the radii of  $\phi$  mesons and  $\Omega$  baryons is studied. The effect due to changes in the strange quark mass is studied in Section VI. Finally, we conclude with a summary in Section VII.

## II. PARTONIC DYNAMICS IN HEAVY-ION COLLISIONS AT RHIC

The dynamical quark coalescence model used in present study requires the space-time and momentum information of quarks and antiquarks during hadronization of the produced QGP in relativistic heavy-ion collisions. In particular, the dynamics of strange and anti-strange quarks are needed for describing the production of  $\phi$  mesons and  $\Omega$  baryons as well as their anisotropic flows, and they are taken from the AMPT model within the string melting scenario [40].

### A. The AMPT model

The AMPT model is a hybrid model that uses minijet partons from hard processes and strings from soft processes in the Heavy Ion Jet Interaction Generator (HIJING) model [41] as the initial conditions for modeling heavy ion collisions at ultra-relativistic energies. Time evolution of resulting minijet partons, which are mostly gluons, is described by Zhang's parton cascade (ZPC) [42] model. At present, this model includes only parton-parton elastic scatterings with in-medium cross sections derived from the lowest-order Born diagrams with an effective gluon screening mass taken as a parameter for fixing the magnitude and angular distribution of parton scattering cross sections. After minijet partons stop interacting, they are combined with their parent strings, as in the HIJING model with jet quenching, to fragment into hadrons using the Lund string fragmentation model as implemented in the PYTHIA program [43]. The final-state hadronic scatterings are modeled by a relativistic transport (ART) model [44].

Since the initial energy density in heavy ion collisions at RHIC is much larger than the critical energy density at which the hadronic matter to quark-gluon plasma transition would occur [45, 46, 47], the AMPT model has been extended by converting the initial excited strings into partons [18]. In this string melting scenario, hadrons, that would have been produced from string fragmentation, are converted instead to their valence quarks and/or antiquarks. Interactions among these quarks are again described by the ZPC parton cascade model. Since inelastic scatterings are not included at present, the resulting partonic matter consists of only quarks and antiquarks from melted strings. To effectively take into account the effect of stronger scattering among gluons if they were present, the scattering cross sections between quarks and antiquarks are taken to be the same as those for gluons. These quarks and antiquarks are converted to hadrons when they stop scattering with other partons. For parton cross sections of about 10 mb, which are used in present study, this criteria for hadronization turns out not too different from the one based on the condition that the local energy density of hadronizing partons drops to a critical energy density given by the lattice QCD calcu-

lations. The transition from the partonic matter to the hadronic matter is achieved using a simple coalescence model, which combines two nearest quark and antiquark into mesons and three nearest quarks or antiquarks into baryons or anti-baryons that are close to the invariant mass of these partons. Details of the AMPT model can be found in Ref. [40].

In the present work, we use the AMPT model in the string melting scenario with the default current quark mass of 9.9 MeV for  $d$  quark, 5.6 MeV for  $u$  quark, and 199 MeV for  $s$  quark and a constant parton cross section of 10 mb. We note that using parton scattering cross sections of 6-10 mb, the AMPT model with string melting was able to reproduce both the centrality and transverse momentum (below 2  $\text{GeV}/c$ ) dependence of the elliptic flow [18] and pion interferometry [48] measured in Au+Au collisions at  $\sqrt{s} = 130$  AGeV at RHIC [49, 50] as well as the measured  $p_T$  dependence of both  $v_2$  and  $v_4$  of mid-rapidity charged hadrons in the same collision at  $\sqrt{s} = 200$  AGeV [27].

### B. Spectrum of strange and antistrange quarks

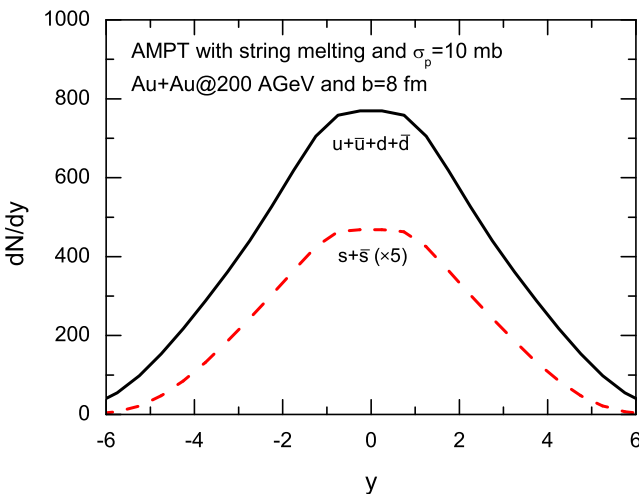


FIG. 1: (Color online) Rapidity distributions of strange and antistrange quarks ( $s + \bar{s}$ ) as well as light quarks and antiquarks ( $u + \bar{u} + d + \bar{d}$ ) at freeze out in Au+Au collisions at  $\sqrt{s_{NN}} = 200$  GeV and  $b = 8$  fm.

We first show in Fig. 1 the rapidity distribution of strange quarks and antiquarks ( $s + \bar{s}$ ) as well as light quarks and antiquarks ( $u + \bar{u} + d + \bar{d}$ ) at freeze out, i.e., stop scattering with other partons, in Au+Au collisions at  $\sqrt{s_{NN}} = 200$  GeV and  $b = 8$  fm. It is seen that the rapidity density  $dN/dy$  at mid-rapidity is about 94 for strange quarks and antiquarks and about 770 for all light quarks and antiquarks. Since inelastic partonic scatterings are absent in the present model, all these quarks and antiquarks are from the melted strings in the initial stage

of the collisions.

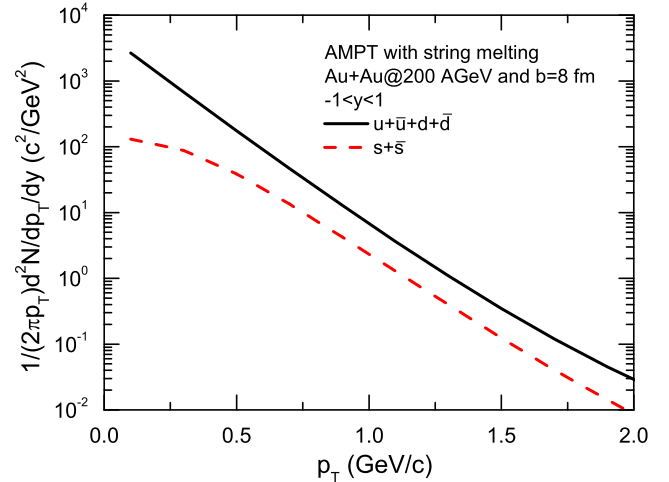


FIG. 2: (Color online) Transverse momentum distributions of mid-rapidity strange and antistrange quarks ( $s + \bar{s}$ ) as well as light quarks and antiquarks ( $u + \bar{u} + d + \bar{d}$ ) at freeze out in Au+Au collisions at  $\sqrt{s_{NN}} = 200$  GeV and  $b = 8$  fm..

The transverse momentum  $p_T$  distributions at midrapidity for strange and antistrange quarks as well as light quarks and antiquarks at freeze out in the same collision are shown in Fig. 2. It clearly shows a quark mass effect as strange and antistrange quarks display a stiffer transverse momentum distribution at lower  $p_T$  compared to that of light quarks and antiquarks. Fitting the transverse momentum spectrum by a Boltzmann distribution, we find that the effective temperature of the partonic matter at freeze out is about 161 MeV, which is consistent with the predicted critical temperature  $T_c \approx 150$ -180 MeV from the lattice QCD for the QGP to hadronic matter phase transition [51, 52].

### C. Space-time structure of strange and antistrange quarks at freeze out

The spatial distribution of mid-rapidity strange and antistrange quarks at freeze out in the above collision is shown in Fig. 3 with the upper panel displaying their number density distribution in the transverse plane and the lower panel giving corresponding contour plot. Here, the transverse plane refers to the  $x$ - $y$  plane with the  $x$ -axis pointing to the direction of the impact parameter and the  $y$ -axis perpendicular to the  $x$ -axis and the  $z$ -axis which is along the beam direction. It is seen that the number density of strange and antistrange quarks at freeze out peaks approximately at a circle with radius of about 4 fm in the transverse plane, implying that these partons mainly freeze out from the surface of an expanding fireball where the number density is roughly between  $1.2 \text{ fm}^{-2}$  and  $1.4 \text{ fm}^{-2}$  in the transverse plane.

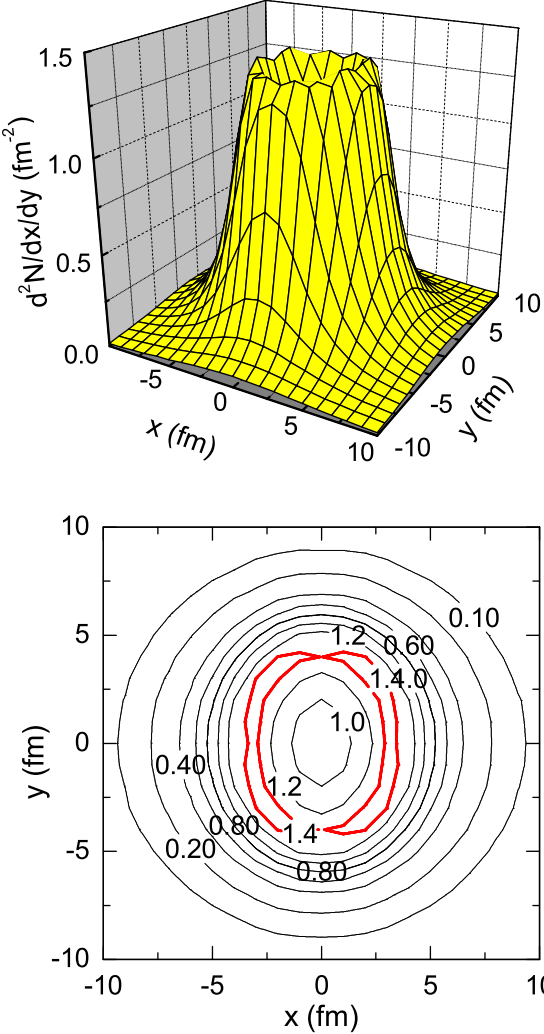


FIG. 3: (Color online) Number density distribution in the transverse plane for mid-rapidity strange and antistrange quarks at freeze out in Au+Au collisions at  $\sqrt{s_{NN}} = 200$  GeV and  $b = 8$  fm (upper panel) and the corresponding contour plot (lower panel).

The space-time structure of the  $z$ - $t$  correlations for mid-rapidity strange and antistrange quarks at freeze out in this collision is shown in Fig. 4. Instead of a sudden freeze out, these partons are seen to freeze out continuously in the proper time  $\tau$ , with most between  $\tau = 4$  and  $6$  fm/c. This can be more clearly seen from their freeze out rate as a function of the proper time  $\tau$  or the time  $t$  in the nucleus-nucleus center of mass system as shown in Fig. 5. From Fig. 5, one can see that the freeze out rate of midrapidity strange and antistrange quarks peaks at  $\tau = 5$  fm/c or  $t = 5.5$  fm/c.

The AMPT model also provides information on the time evolution of the parton energy density. This is shown in Fig. 6 for the central cell of the partonic matter in above collision. As in Refs. [45, 46], the central cell is

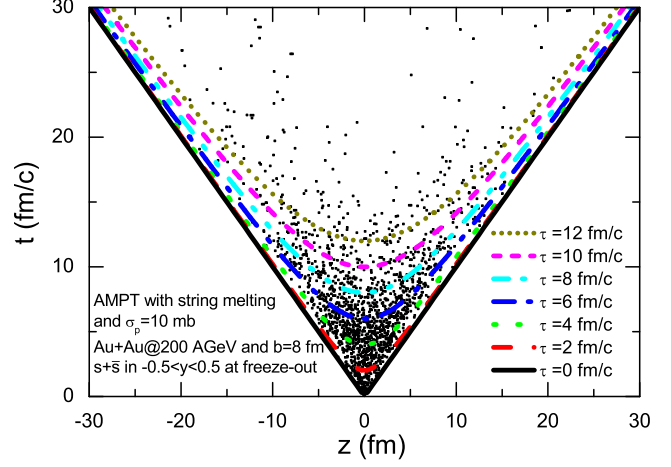


FIG. 4: (Color online) Space-time structure of mid-rapidity strange and antistrange quarks at freeze out in Au+Au collisions at  $\sqrt{s_{NN}} = 200$  GeV and  $b = 8$  fm.

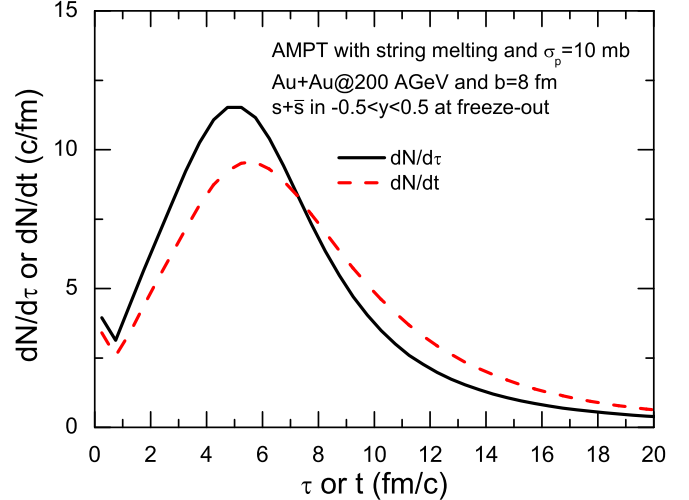


FIG. 5: (Color online) Freeze out rate of mid-rapidity strange and antistrange quarks as a function of proper time  $\tau$  as well as the time  $t$  in the nucleus-nucleus center of mass system.

taken to have a transverse radius of 1 fm and a longitudinal dimension of 5% of the time  $t$  after the two nuclei have fully overlapped in the longitudinal direction. It is seen that the central energy density is about  $0.6$  GeV/fm $^3$  at  $t = 5.5$  fm/c when most of partons freeze out. This energy density is consistent with the critical energy density of about  $0.66$  GeV/fm $^3$  predicted by the lattice QCD for the quark-gluon plasma to hadronic matter transition [51, 52].

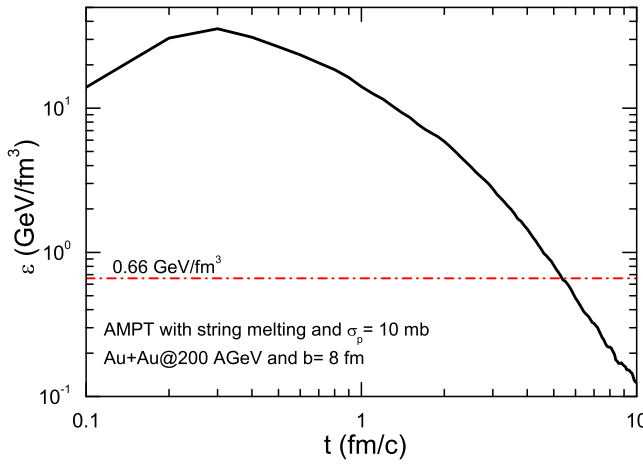


FIG. 6: (Color online) Time evolution of the energy density in the central cell of the partonic matter in Au+Au collisions at  $\sqrt{s_{NN}} = 200$  GeV and  $b = 8$  fm.

#### D. Anisotropic flow of strange and antistrange quarks

The anisotropy in the transverse momentum distribution of particles in non-central heavy ion collisions is generated by the pressure anisotropy in the initial compressed matter [53, 54] and thus depends on the geometry and energy density as well as the properties of produced matter during the early stage of these collisions. For  $\phi$  mesons and  $\Omega$  baryons, their anisotropic flows are essentially determined by those of strange and antistrange quarks at freeze out and their hadronization mechanism. As discussed previously, the effect due to later hadronic matter is small because the pressure becomes more isotropic in hadronic matter and also the interactions of  $\phi$  mesons and  $\Omega$  baryons in the hadronic matter are relatively weak.

From the momentum distribution of strange and antistrange quarks at freeze out, their elliptic and fourth-order anisotropic flows can be evaluated according to following single-particle averages:

$$v_2(p_T) = \left\langle \frac{p_x^2 - p_y^2}{p_T^2} \right\rangle \quad (1)$$

$$v_4(p_T) = \left\langle \frac{p_x^4 - 6p_x^2p_y^2 + p_y^4}{p_T^4} \right\rangle \quad (2)$$

where  $p_x$  and  $p_y$  are, respectively, projections of their momentum in and perpendicular to the reaction plane, and  $p_T = (p_x^2 + p_y^2)^{1/2}$  is the transverse momentum.

In Fig. 7, we show the  $p_T$  dependence of  $v_2$  and  $v_4$  of mid-rapidity strange and antistrange quarks ( $s + \bar{s}$ ) at freeze out in Au+Au collisions at  $\sqrt{s_{NN}} = 200$  GeV and  $b = 8$  fm. It is seen that strange and antistrange quarks exhibit not only a strong  $v_2$  but also a non-negligible  $v_4$

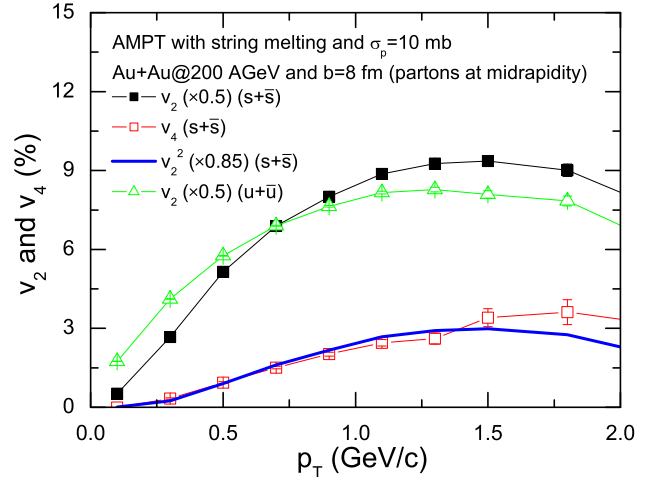


FIG. 7: (Color online) Transverse momentum ( $p_T$ ) dependence of elliptic flow  $v_2$  (solid squares) and forth-order anisotropic flow  $v_4$  (open squares) of mid-rapidity strange and antistrange quarks ( $s + \bar{s}$ ) at freeze out in Au+Au collisions at  $\sqrt{s_{NN}} = 200$  GeV and  $b = 8$  fm. The thick solid line represents  $0.85v_2^2$ . Also included is  $v_2$  (open triangles) of mid-rapidity light up and anti-up quarks ( $u + \bar{u}$ ).

that approximately scales with  $v_2^2$  with a scaling coefficient of 0.85, i.e.,  $v_4 \sim 0.85v_2^2$  as shown by the thick solid line in Fig. 7. Compared to the  $v_2$  of mid-rapidity light up and anti-up quarks ( $u + \bar{u}$ ), shown by triangles in Fig. 7, the  $v_2$  of heavier strange and antistrange quarks has a smaller value at low  $p_T$  but a larger value at high  $p_T$ , similar to the mass ordering of hadron elliptic flows in the hydrodynamic model which assumes that the matter is in local thermal equilibrium and thus develops a large collective radial flow. However, instead of a continuing increase of  $v_2$  with respect to  $p_T$  as in the hydrodynamic model, the  $v_2$  of partons in the transport model saturates at a maximum value when their  $p_T$  becomes large, indicating that high momentum partons do not reach thermal equilibrium with the bulk of the partonic matter.

#### III. A DYNAMICAL QUARK COALESCENCE MODEL FOR $\phi$ AND $\Omega$ PRODUCTION

In the coalescence model, the probability for forming a bound cluster from a many-particle system is determined by the overlap of the wave function of coalescing particles with the internal wave function of the cluster. Its validity is based on the assumption that coalescing particles are statistically independent and binding energies of formed clusters as well as the quantum dynamics for the coalescing process only play minor roles [55]. In the present study, we assume that correlations among partons at freeze out are weak and binding energies of formed hadrons can be neglected. Furthermore, the coalescence model is considered as a perturbative approach,

valid only if the number of partons coalesced into hadrons is small compared with the total number of partons in the system. As shown later, this condition is satisfied for  $\phi$  mesons and  $\Omega$  baryons produced in relativistic heavy ion collisions as their numbers are small compared with that of strange and antistrange quarks.

### A. The dynamical coalescence model

In the dynamical quark coalescence model, the probability for producing a hadron from partons in the QGP is given by the overlap of parton phase-space distributions at freeze out with the parton Wigner phase-space function inside the hadron. For a QGP containing  $A$  partons, the momentum distribution of a  $M$ -parton hadron can be expressed as [55, 56]

$$\frac{dN_M}{d^3K} = G \left( \frac{A}{M} \right) \frac{1}{A^M} \int \prod_{i=1}^M f_i(\mathbf{r}_i, \mathbf{k}_i) \times \rho^W(\mathbf{r}_{i_1}, \mathbf{k}_{i_1} \cdots \mathbf{r}_{i_{M-1}}, \mathbf{k}_{i_{M-1}}) \times \delta(\mathbf{K} - (\mathbf{k}_1 + \cdots + \mathbf{k}_M)) d\mathbf{r}_1 d\mathbf{k}_1 \cdots d\mathbf{r}_M d\mathbf{k}_M, \quad (3)$$

where  $f_i$  is the parton phase-space distribution functions at freeze-out;  $\rho^W$  is the  $M$ -parton Wigner phase-space function inside the hadron;  $\mathbf{r}_{i_1}, \dots, \mathbf{r}_{i_{M-1}}$  and  $\mathbf{k}_{i_1}, \dots, \mathbf{k}_{i_{M-1}}$  are, respectively, the  $M-1$  relative coordinates and momenta taken at equal time in the  $M$ -parton rest frame ( $\mathbf{K} = \mathbf{0}$ ); and  $G$  is the statistical factor for the  $M$  partons to form the hadron.

In transport model simulations for hadron production from the dynamical quark coalescence model in heavy ion collisions, the multiplicity of a  $M$ -parton hadron is then given by [55, 56]

$$N_M = G \int \sum_{i_1 > i_2 > \dots > i_M} d\mathbf{r}_{i_1} d\mathbf{k}_{i_1} \cdots d\mathbf{r}_{i_{M-1}} d\mathbf{k}_{i_{M-1}} \times \langle \rho_i^W(\mathbf{r}_{i_1}, \mathbf{k}_{i_1} \cdots \mathbf{r}_{i_{M-1}}, \mathbf{k}_{i_{M-1}}) \rangle, \quad (4)$$

where  $\langle \dots \rangle$  denotes event averaging and the sum runs over all possible combinations of  $M$  partons.

To determine the statistical factor  $G$  for the  $\phi$  meson, we note that the quark wave function of a  $\phi$  meson in the color-spin-isospin space can be expressed as a linear combination of all possible orthogonal flavor, color, and spin basis states [1, 57]. The probability for a strange quark  $s$  and an anti-strange quark  $\bar{s}$  to form a hadron with quantum numbers corresponding to a  $\phi$  meson with the  $z$ -component of its spin equal to 1 is simply given by the probability of finding the two  $s$  and  $\bar{s}$  in any one of these color-spin-isospin basis states, i.e.,  $1/3^2 \times 1/2^2 = 1/36$ . Including also the possibility of forming a  $\phi$  with the  $z$ -component of its spin equal to  $-1$  and  $0$  triples the probability. As a result, the statistical factor  $G$  for the  $\phi$  meson is  $1/12$ . A similar consideration leads to a statistical factor  $G = 1/54$  for the  $\Omega^-$  and  $\bar{\Omega}^+$  baryons.

### B. Parton phase-space distributions

The  $M$ -parton phase-space distribution function  $\prod_{i=1}^M f_i(\mathbf{r}_i, \mathbf{k}_i)$  in Eq. (3) refers to partons with spatial coordinates and momenta at equal time in the rest frame of the  $M$ -parton cluster. Since parton momenta in the AMPT model are given in the nucleus-nucleus center of mass system, a Lorentz transformation is performed to obtain their momenta in the rest frame of the  $M$ -parton cluster. Furthermore, partons freeze out at different times as shown in Figs. 4 and 5. The same Lorentz transformation is thus used in obtaining their space-time coordinates in the rest frame of the  $M$ -parton cluster. To determine the spatial coordinates of these partons at equal time in their rest frame, partons in the cluster that freeze out earlier are allowed to propagate freely, i.e., with constant velocities given by the ratio of their momenta and energies in the rest frame of the cluster, until the time when the last parton in the cluster freezes out.

### C. Quark Wigner phase-space functions inside $\phi$ and $\Omega$

To determine the quark Wigner phase-space functions inside hadrons requires knowledge of their quark wave functions. For the  $\phi$  meson, we take its quark wave function to be that of a spherical harmonic oscillator, i.e.,

$$\psi(\mathbf{r}_1, \mathbf{r}_2) = 1/(\pi\sigma_\phi^2)^{3/4} \exp(-r^2/(2\sigma_\phi^2)), \quad (5)$$

in terms of the relative coordinate  $\mathbf{r} = \mathbf{r}_1 - \mathbf{r}_2$  and the size parameter  $\sigma_\phi$ . The above normalized wave function leads to a root mean-square radius  $R_\phi = \langle r^2 \rangle^{1/2} = (3/8)^{1/2} \sigma_\phi$  for the  $\phi$  meson.

The quark Wigner phase-space function inside the  $\phi$  meson is obtained from its quark wave function by

$$\begin{aligned} \rho_\phi^W(\mathbf{r}, \mathbf{k}) &= \int \psi\left(\mathbf{r} + \frac{\mathbf{R}}{2}\right) \psi^*\left(\mathbf{r} - \frac{\mathbf{R}}{2}\right) \exp(-i\mathbf{k} \cdot \mathbf{R}) d^3\mathbf{R} \\ &= 8 \exp\left(-\frac{r^2}{\sigma_\phi^2} - \sigma_\phi^2 k^2\right) \end{aligned} \quad (6)$$

where  $\mathbf{k} = (\mathbf{k}_1 - \mathbf{k}_2)/2$  is the relative momentum between the  $s$  and  $\bar{s}$  quarks.

For  $\Omega^-$  and  $\bar{\Omega}^+$  baryons, their quark wave functions are taken to be the same and are given by that of a spherical harmonic oscillator as well [58, 59], i.e.,

$$\psi(\mathbf{r}_1, \mathbf{r}_2, \mathbf{r}_3) = (3\pi^2\sigma_\Omega^4)^{-3/4} \exp\left(-\frac{\rho^2 + \lambda^2}{2\sigma_\Omega^2}\right), \quad (7)$$

in terms of the relative coordinates  $\rho$  and  $\lambda$ , and the size parameter  $\sigma_\Omega$ . In the above, we have used the normal

Jacobi coordinates for a three-particle system [56], i.e.,

$$\begin{pmatrix} \mathbf{R} \\ \rho \\ \lambda \end{pmatrix} = \begin{pmatrix} \frac{1}{3} & \frac{1}{3} & \frac{1}{3} \\ \frac{1}{\sqrt{2}} & -\frac{1}{\sqrt{2}} & 0 \\ \frac{1}{\sqrt{6}} & \frac{1}{\sqrt{6}} & -\frac{2}{\sqrt{6}} \end{pmatrix} \begin{pmatrix} \mathbf{r}_1 \\ \mathbf{r}_2 \\ \mathbf{r}_3 \end{pmatrix}, \quad (8)$$

where  $\mathbf{R}$  is the center-of-mass coordinate of the three quarks or antiquarks.

Using  $d\mathbf{r}_1 d\mathbf{r}_2 d\mathbf{r}_3 = 3^{3/2} d\mathbf{R} d\rho d\lambda$ , it is easy to check that the wave function given by Eq. (7) is normalized to one. From the relation  $(\mathbf{r}_1 - \mathbf{R})^2 + (\mathbf{r}_2 - \mathbf{R})^2 + (\mathbf{r}_3 - \mathbf{R})^2 = \rho^2 + \lambda^2$ , the root mean-square radius  $R_\Omega$  of the  $\Omega$  baryon is given by

$$R_\Omega = \left[ \int \frac{\rho^2 + \lambda^2}{3} |\psi(\mathbf{r}_1, \mathbf{r}_2, \mathbf{r}_3)|^2 3^{3/2} d\rho d\lambda \right]^{1/2} = \sigma_\Omega. \quad (9)$$

The quark Wigner phase-space function inside the  $\Omega$  baryon is obtained from its quark wave function via

$$\begin{aligned} & \rho_\Omega^W(\rho, \lambda, \mathbf{k}_\rho, \mathbf{k}_\lambda) \\ &= \int \psi \left( \rho + \frac{\mathbf{R}_1}{2}, \lambda + \frac{\mathbf{R}_2}{2} \right) \psi^* \left( \rho - \frac{\mathbf{R}_1}{2}, \lambda - \frac{\mathbf{R}_2}{2} \right) \\ & \quad \times \exp(-i\mathbf{k}_\rho \cdot \mathbf{R}_1) \exp(-i\mathbf{k}_\lambda \cdot \mathbf{R}_2) 3^{3/2} d\mathbf{R}_1 d\mathbf{R}_2 \\ &= 8^2 \exp \left( -\frac{\rho^2 + \lambda^2}{\sigma_\Omega^2} \right) \exp(-(\mathbf{k}_\rho^2 + \mathbf{k}_\lambda^2)\sigma_\Omega^2), \end{aligned} \quad (10)$$

where  $\mathbf{k}_\rho$  and  $\mathbf{k}_\lambda$  are relative momenta, which together with the total momentum  $\mathbf{K}$  are defined by [56]

$$\begin{pmatrix} \mathbf{K} \\ \mathbf{k}_\rho \\ \mathbf{k}_\lambda \end{pmatrix} = \begin{pmatrix} 1 & 1 & 1 \\ \frac{1}{\sqrt{2}} & -\frac{1}{\sqrt{2}} & 0 \\ \frac{1}{\sqrt{6}} & \frac{1}{\sqrt{6}} & -\frac{2}{\sqrt{6}} \end{pmatrix} \begin{pmatrix} \mathbf{k}_1 \\ \mathbf{k}_2 \\ \mathbf{k}_3 \end{pmatrix}, \quad (11)$$

with  $\mathbf{k}_1$ ,  $\mathbf{k}_2$ , and  $\mathbf{k}_3$  being momenta of the three quarks.

#### D. $\phi$ and $\Omega$ size parameters

The two parameters  $\sigma_\phi$  and  $\sigma_\Omega$  in the quark Wigner phase-space functions inside the  $\phi$  meson and  $\Omega$  baryon are related to their root-mean-square radii. Since the latter are not known empirically, we take them as adjustable parameters and fix them from fitting the measured yields of  $\phi$  mesons and  $\Omega$  baryons in relativistic heavy ion collisions.

For  $\phi$  mesons, experimental data on the rapidity density  $dN/dy$  at mid-rapidity and its centrality dependence are available for Au+Au collisions at  $\sqrt{s_{NN}} = 200$  GeV [37, 38]. There is, however, a significant difference between the STAR and PHENIX data for the  $\phi$  meson yield. For instance, the  $\phi$  meson  $dN/dy$  at mid-rapidity is about 7.7 in the STAR data while 4.5 in the PHENIX data for Au+Au collisions at  $\sqrt{s_{NN}} = 200$  GeV with a centrality of 0-5%. Using the above described dynamical quark coalescence model, we find that the STAR (PHENIX) data can be approximately reproduced with a  $\phi$  meson size

parameter  $\sigma_\phi \approx 1.06$  (0.77) fm, which gives a reasonable  $\phi$  meson root-mean-square radius of about  $R_\phi = 0.65$  (0.47) fm. For the impact parameter  $b = 8$  fm as mainly considered in present study, the AMPT model gives the number of participant nucleons  $N_{\text{part}} \approx 160$  which corresponds to a centrality of about 31%. The resulting  $\phi$  meson rapidity density  $dN/dy$  at mid-rapidity obtained with  $\phi$  the meson radius  $R_\phi = 0.65$  (0.47) fm is about 3.3 (2.0), which is also in good agreement with the experimental data [37, 38].

For  $\Omega$  baryons, there are only preliminary experimental data on its  $dN/dy$  at mid-rapidity in central collisions of Au+Au at  $\sqrt{s_{NN}} = 200$  GeV, and its value is about 0.64 [39]. Fitting the result from the present dynamical quark coalescence model for the same collision at  $b = 0$  fm leads to a  $\Omega$  baryon size parameter  $\sigma_\Omega \approx 1.2$  fm, corresponding to a  $\Omega$  baryon root-mean-square radius of about  $R_\Omega \approx 1.2$  fm, which is somewhat large but not unrealistic. For more peripheral collisions at impact parameter  $b = 8$  fm, an  $\Omega$  radius of  $R_\Omega = 1.2$  fm leads to a rapidity density  $dN/dy$  of about 0.26 at mid-rapidity.

In the following, we shall use the above determined root mean-square radii for  $\phi$  mesons and  $\Omega$  baryons, i.e.,  $R_\phi = 0.65$  fm or 0.47 fm for the  $\phi$  meson while  $R_\Omega = 1.2$  fm for the  $\Omega$  baryon unless stated otherwise.

### IV. $\phi$ AND $\Omega$ PRODUCTION IN AU+AU COLLISIONS AT $\sqrt{s_{NN}} = 200$ GeV

Using the phase-space information and the dynamical coalescence model described above, we can now study the transverse momentum spectra of  $\phi$  mesons and  $\Omega$  baryons as well as their anisotropic flows in relativistic heavy ion collisions.

#### A. Transverse momentum spectra of $\phi$ and $\Omega$

Fig. 8 shows the transverse momentum spectra of midrapidity  $\phi$  mesons and  $\Omega$  baryons as well as their ratio in Au+Au collisions at  $\sqrt{s_{NN}} = 200$  GeV with  $b = 0$  fm (left panels) and  $b = 8$  fm (right panels), and  $R_\phi = 0.65$  fm or 0.47 fm and  $R_\Omega = 1.2$  fm. For comparison, we also include in up-left panel of Fig. 8 the experimental data for  $\phi$  mesons in 0-5% centrality bin from the STAR collaboration [37] (solid stars) and in 0-10% centrality bin from the PHENIX collaboration [38] (open stars) as well as the preliminary data for  $\Omega$  baryons in 0-10% centrality bin from the STAR collaboration [39] (solid triangles). Also shown in lower left panel by open triangles are the data on the  $\Omega/\phi$  ratio in 0-10% centrality bin, obtained from a linear interpolation of the  $\phi$  meson data in upper left panel.

It is seen from upper left panel of Fig. 8 that the calculated transverse momentum spectrum of  $\Omega$  baryons is stiffer than that of  $\phi$  mesons as expected from the difference in their masses. Both calculated transverse

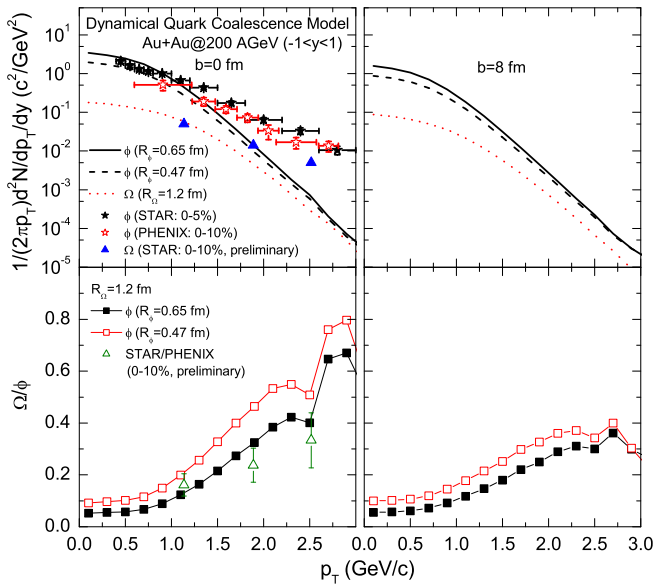


FIG. 8: (Color online)  $p_T$ -dependence of midrapidity  $\phi$  mesons and  $\Omega$  ( $\Omega^- + \bar{\Omega}^+$ ) baryons (upper panels) and their ratio (lower panels) in Au+Au collisions at  $\sqrt{s_{NN}} = 200$  GeV with  $b = 0$  fm (left panels) and  $b = 8$  fm (right panels). Also included in up-left panel are the data for  $\phi$  mesons in 0-5% centrality bin from the STAR collaboration [37] (solid stars) and in 0-10% centrality bin from the PHENIX collaboration [38] (open stars) as well as preliminary data for  $\Omega$  baryons in 0-10% centrality bin from the STAR collaboration [39] (solid triangles). Data for the  $\Omega/\phi$  ratio in 0-10% centrality bin are also shown in the lower-left panel.

momentum spectra of  $\phi$  mesons and  $\Omega$  baryons are, however, significantly softer than the data. With  $R_\phi = 0.65$  (0.47) fm, the mean transverse momentum  $\langle p_T \rangle$  calculated from the  $\phi$  meson transverse momentum spectrum is about 0.72 (0.73) and 0.68 (0.70) GeV/c for  $b = 0$  fm and  $b = 8$  fm, respectively, which are significantly smaller than the experimental value of about 0.85-1.1 GeV/c [37, 38]. For  $\Omega$  baryons, their mean transverse momentum  $\langle p_T \rangle$  is about 0.93 and 0.83 GeV/c for  $b = 0$  fm and  $b = 8$  fm, respectively, and are larger than those of  $\phi$  mesons.

We note that hadron transverse momentum spectra obtained from the AMPT model with string melting are generally softer than those measured in experiments [60]. Since the hadron spectra reflect those of partons in the parton coalescence model, soft hadron spectra are due to soft parton spectra during the partonic stage. As discussed in Ref. [60], the latter is a result of using the small current quark masses in the parton cascade of the AMPT model with string melting, which make their transverse momentum spectra less affected by the radial collective flow than hadrons in the default AMPT model. Since anisotropic flows are given by ratios of hadron transverse momentum spectra, predictions of anisotropic flows as well as the ratio of hadron transverse momentum spectra

from the present model are expected to be more reliable [18, 60].

The transverse momentum dependence of the ratio of midrapidity  $\Omega$  baryons to  $\phi$  mesons shown in the lower panels of Fig. 8 is seen to increase appreciably from low  $p_T$  to the intermediate  $p_T$  of about 2.5 GeV/c. The enhancement factor is about 7 and 4 for  $b = 0$  fm and  $b = 8$  fm, respectively. This enhancement is a result of parton coalescence as in the case of the observed anomalously large anti-proton to pion ratio of about 0.8 and 0.4 at  $p_T \gtrsim 2.5$  GeV/c in central and mid-peripheral (centrality of about 30%) Au+Au collisions at  $\sqrt{s_{NN}} = 200$  GeV, respectively [61]. As explained in Refs. [1, 2, 3], in the coalescence model baryons with transverse momentum  $p_T$  are mainly formed from quarks with transverse momenta  $\sim p_T/3$ , while mesons with same transverse momentum are mainly produced from partons with transverse momenta  $\sim p_T/2$ . Since quark transverse momentum spectra decrease with  $p_T$ , it is more favorable to produce high transverse momentum baryons than mesons if hadrons are produced from the QGP through the coalescence of quarks. In the present study, the  $\bar{\Omega}^+/\phi$  is about 0.25 and 0.17 at  $p_T \approx 2.5$  GeV/c for  $b = 0$  fm and  $b = 8$  fm, respectively, which are significantly smaller than those of anti-protons to pions observed in experiments. For  $b = 0$ , our result with  $R_\phi = 0.65$  fm reproduces reasonably the measured  $\Omega/\phi$  ratio as shown in the lower left panel of Fig. 8.

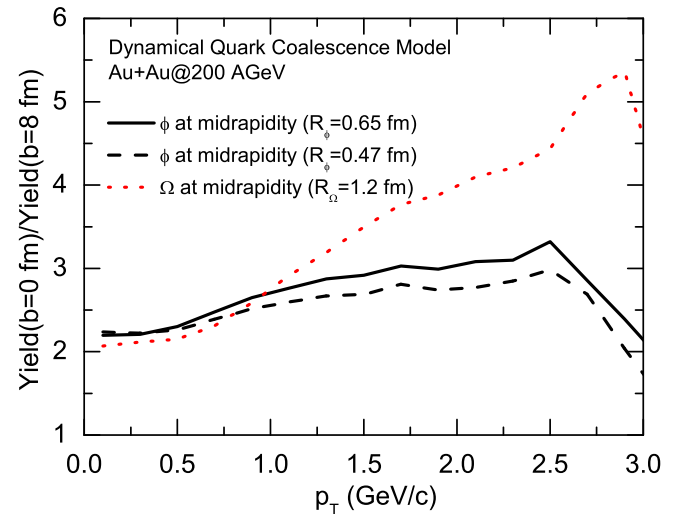


FIG. 9: (Color online)  $p_T$ -dependence of the yield ratio of midrapidity  $\phi$  mesons and  $\Omega$  baryons in central ( $b = 0$  fm) to that in mid-peripheral ( $b = 8$  fm) Au+Au collisions at  $\sqrt{s_{NN}} = 200$  GeV.

In Fig. 9, we show the  $p_T$  dependence of the yield ratio of midrapidity  $\phi$  mesons and  $\Omega$  baryons in central ( $b = 0$  fm) to that in mid-peripheral ( $b = 8$  fm) collisions of Au+Au at  $\sqrt{s_{NN}} = 200$  GeV. It is seen that the  $p_T$  dependence is very different for  $\phi$  mesons and  $\Omega$  baryons

with  $\Omega$  baryons having a smaller value at low  $p_T$  while a larger value at high  $p_T$  than  $\phi$  mesons. Our results thus indicate that nuclear suppression at intermediate momenta is weaker for  $\Omega$  baryons than  $\phi$  mesons. This feature is consistent with the experimental data for the  $p_T$  dependence of the so-called  $R_{CP}$  for  $p + \bar{p}$  and pions [61].

### B. Anisotropic flows of $\phi$ and $\Omega$

In heavy-ion collisions at RHIC, experimental data have indicated that there exist not only strong elliptic flow but also a clear fourth-order anisotropic flow  $v_4$  for charged hadrons [26]. An interesting finding about  $v_4$  is that it scales with the square of  $v_2$ , i.e.,  $v_4(p_T) \sim v_2^2(p_T)$ . In the present subsection, the elliptic and fourth-order anisotropic flows of  $\phi$  mesons and  $\Omega$  baryons are studied to see if they also show similar features.

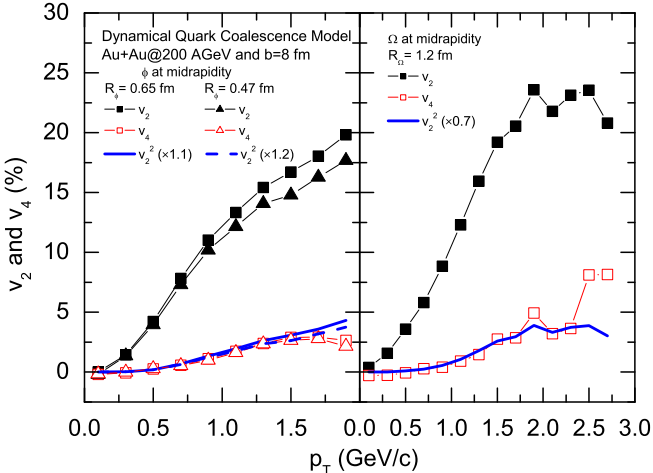


FIG. 10: (Color online)  $p_T$ -dependence of the anisotropic flows  $v_2$  and  $v_4$  of mid-rapidity  $\phi$  mesons (left panel) and  $\Omega$  baryons (right panel) produced in Au+Au collisions at  $\sqrt{s_{NN}} = 200$  GeV and  $b = 8$  fm. Also shown are  $1.1v_2^2$  (solid line in left panel) and  $1.2v_2^2$  (dashed line in left panel) for  $\phi$  mesons, and  $0.7v_2^2$  (solid line in right panel) for  $\Omega$  baryons.

In left panel of Fig. 10, we show the  $p_T$  dependence of the anisotropic flows  $v_2$  and  $v_4$  of mid-rapidity  $\phi$  mesons produced in Au+Au collisions at  $\sqrt{s_{NN}} = 200$  GeV and  $b = 8$  fm. Solid and open squares are, respectively, the  $\phi$  meson  $v_2$  and  $v_4$  for a  $\phi$  meson radius  $R_\phi = 0.65$  fm, while solid and open triangles are, respectively, those for  $R_\phi = 0.47$  fm. It is seen that the scaling relation  $v_4(p_T) \sim v_2^2(p_T)$  is satisfied in both cases as shown by the solid ( $1.1v_2^2$ ) and dashed ( $1.2v_2^2$ ) lines in the same figure. Similar results for  $\Omega$  baryons using the radius  $R_\Omega = 1.2$  fm are shown in right panel of Fig. 10. The scaling relation  $v_4(p_T) \sim v_2^2(p_T)$  is again satisfied for  $\Omega$  baryons but with a smaller scaling coefficient than that

for  $\phi$  mesons as shown by the solid line ( $0.7v_2^2$ ) in the right panel.

Based on the naive momentum-space quark coalescence model that only allows quarks with equal momentum to form a hadron [4], this scaling relation between hadron  $v_2(p_T)$  and  $v_4(p_t)$  has been attributed to a similar scaling relation between those of quarks [27, 28]. Neglecting the small contribution of higher-order anisotropic flows (higher than forth-order), this model gives for mid-rapidity hadrons

$$\begin{aligned} \frac{v_{4,M}(2p_T)}{v_{2,M}^2(2p_T)} &\approx \frac{1}{4} + \frac{1}{2} \frac{v_{4,q}(p_T)}{v_{2,q}^2(p_T)}, \\ \frac{v_{4,B}(3p_T)}{v_{2,B}^2(3p_T)} &\approx \frac{1}{3} \left( 1 + \frac{v_{4,q}(p_T)}{v_{2,q}^2(p_T)} \right), \end{aligned} \quad (12)$$

where  $v_{n,M}(p_T)$ ,  $v_{n,B}(p_T)$  and  $v_{n,q}(p_T)$  denote, respectively, the meson, baryon, and quark anisotropic flows. The hadron anisotropic flows thus satisfy the scaling relation  $v_4(p_T) \sim v_2^2(p_T)$  if a similar scaling relation is satisfied by the quark anisotropic flows.

We have already shown in Fig. 7 that the scaling relation  $v_4(p_T) \sim v_2^2(p_T)$  is satisfied by the mid-rapidity strange and antistrange quarks ( $s + \bar{s}$ ) with a scaling coefficient of about 0.85, i.e.,  $v_{4,q}(p_T)/v_{2,q}^2(p_T) \approx 0.85$ . Eq. (12) then leads to a scaling coefficient of  $v_{4,\phi}(p_T)/v_{2,\phi}^2(p_T) \approx 0.68$  for  $\phi$  mesons and  $v_{4,\Omega}(p_T)/v_{2,\Omega}^2(p_T) \approx 0.62$  for  $\Omega$  baryons. Comparing with the scaling coefficients of 1.1 or 1.2 for  $\phi$  mesons and 0.7 for  $\Omega$  baryons from the dynamical quark coalescence model, the predicted value from the naive momentum-space quark coalescence model for the  $\phi$  meson scaling coefficient is significantly smaller. However, the dynamical quark coalescence model does give a larger scaling coefficient for  $\phi$  mesons than for  $\Omega$  baryons as expected from the naive momentum-space coalescence model.

Another interesting and important finding in heavy-ion collisions at RHIC is the valence quark number scaling of the elliptic flow of identified hadrons, i.e., the elliptic flow per valence quark in a hadron is same at same transverse momentum per valence quark, i.e.,  $v_{2,H}(p_T/n_q)/n_q = v_{2,q}(p_T)$  with  $v_{2,H}$  and  $n_q$  denoting, respectively, the hadron  $v_2$  and the number of valence quarks or anti-quarks in a hadron. In the naive momentum-space quark coalescence model, this scaling has been shown to be exactly satisfied [4, 28]. The scaling is, however, broken in more general quark coalescence models that take into account the quark momentum distribution [62, 63, 64] and higher parton Fock states [65] in hadrons as well as the effect of resonance decays [62]. It is thus of interest to see if the elliptic flows of  $\phi$  mesons and  $\Omega$  baryons from present dynamical quark coalescence model also satisfy the valence quark number scaling.

In Fig. 11, we show the  $p_T/n_q$ -dependence of  $v_2$  per valence quark or anti-quark in a hadron for mid-rapidity  $\phi$  mesons and  $\Omega$  baryons produced in Au+Au collisions at  $\sqrt{s_{NN}} = 200$  GeV and  $b = 8$  fm with  $R_\phi = 0.47$  or 0.65 fm and  $R_\Omega = 1.2$  fm. For comparison, we also include

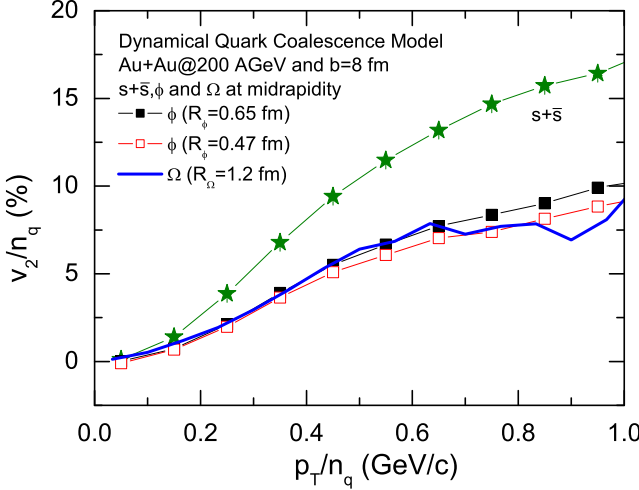


FIG. 11: (Color online)  $p_T/n_q$ -dependence of  $v_2$  per valence quark or anti-quark in a hadron for mid-rapidity  $\phi$  mesons and  $\Omega$  baryons produced in Au+Au collisions at  $\sqrt{s_{NN}} = 200$  GeV and  $b = 8$  fm with  $R_\phi = 0.65$  fm (solid squares) and  $0.47$  fm (open squares) as well as  $R_\Omega = 1.2$  fm (solid line). The results of mid-rapidity strange and antistrange quarks ( $s + \bar{s}$ ) at freeze-out are shown by solid stars.

the elliptic flow of mid-rapidity strange and antistrange quarks ( $s + \bar{s}$ ) at freeze-out. It is seen that the elliptic flows of both mid-rapidity  $\phi$  mesons and  $\Omega$  baryons from the dynamical quark coalescence model satisfy the valence number scaling. The valence-quark-number-scaled  $v_2$  is, however, significantly smaller than the  $v_2$  of coalescing strange and antistrange quarks. This feature is different from the prediction of the naive momentum-space quark coalescence model where the valence-quark-number-scaled  $v_2$  is equal to the  $v_2$  of coalescing strange quarks and anti-quarks. Our results therefore indicate that both the dynamical phase-space information of quarks and the quark phase-space distribution inside hadrons play important roles in hadron anisotropic flows, and cautions are needed in interpreting the elliptic flow of partons from that of hadrons using the naive momentum-space parton coalescence model. We note that our results are consistent with previous studies on the  $v_2$  of protons and pions based on the parton phase-space information from the MPC parton cascade model [5].

## V. HADRON SIZE DEPENDENCE OF $\phi$ AND $\Omega$ YIELDS AND ANISOTROPIC FLOWS

In above calculations, we have used the size parameters of  $\phi$  mesons and  $\Omega$  baryons that are fixed from fitting the measured yields in experiments. Ideally, we would like use the empirically and/or theoretical determined root-mean-square radii for the  $\phi$  meson and  $\Omega$  baryon in the dynamical quark coalescence model. In the absence of

such information, it is of interest to study how above results depend on the sizes of  $\phi$  mesons and  $\Omega$  baryons.

### A. Hadron size dependence of $\phi$ and $\Omega$ yields

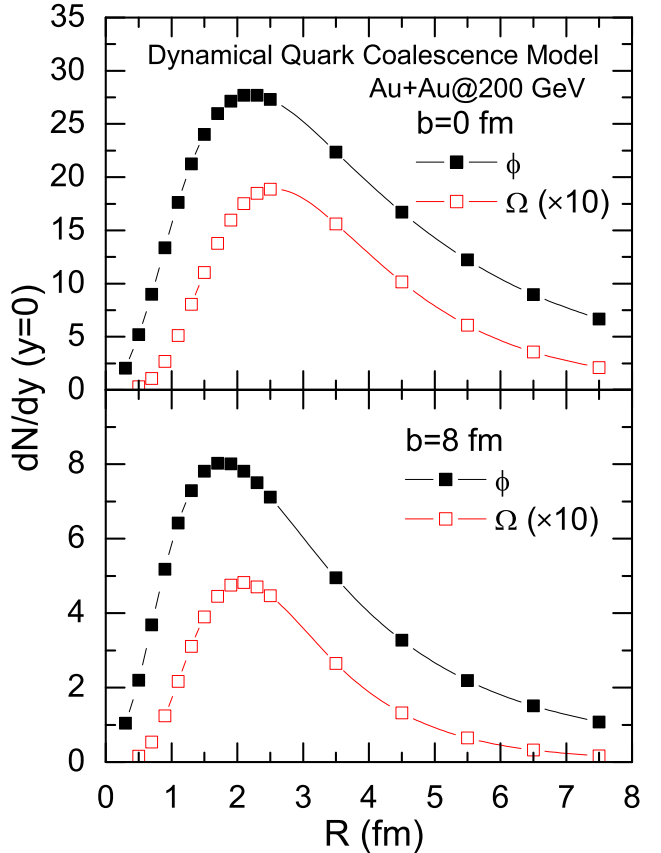


FIG. 12: (Color online) Hadron size (root-mean-square radius) dependence of rapidity density  $dN/dy$  at mid-rapidity for  $\phi$  mesons (solid squares) and  $\Omega$  ( $\Omega^- + \bar{\Omega}^+$ ) baryons (open squares) produced in Au+Au collisions at  $\sqrt{s_{NN}} = 200$  GeV with  $b = 0$  fm (upper panel) and  $b = 8$  fm (lower panel).

We show in Fig. 12 the rapidity density  $dN/dy$  at mid-rapidity for  $\phi$  mesons and  $\Omega$  baryons produced in Au+Au collisions at  $\sqrt{s_{NN}} = 200$  GeV with  $b = 0$  fm (upper panel) and  $b = 8$  fm (lower panel) as functions of their root-mean-square radii. It is seen that both the yield of  $\phi$  mesons and that of  $\Omega$  baryons are very sensitive to their sizes. For physically reasonable radii, both yields of  $\phi$  mesons and  $\Omega$  baryons increase with increasing radii. Their yields eventually decrease as the radii become unrealistically large. For collisions at impact parameter  $b = 0$  fm, the yield exhibits a maximum at  $R_\phi = 2.2$  fm for  $\phi$  mesons and at  $R_\Omega = 2.5$  fm for  $\Omega$  baryons. A similar feature is observed in the case of  $b = 8$  fm but the maximum is at  $R_\phi = 1.75$  fm for  $\phi$  mesons and at  $R_\Omega = 2$  fm for  $\Omega$  baryons.

## B. Hadron size dependence of $\phi$ and $\Omega$ elliptic flows and the valence quark number scaling

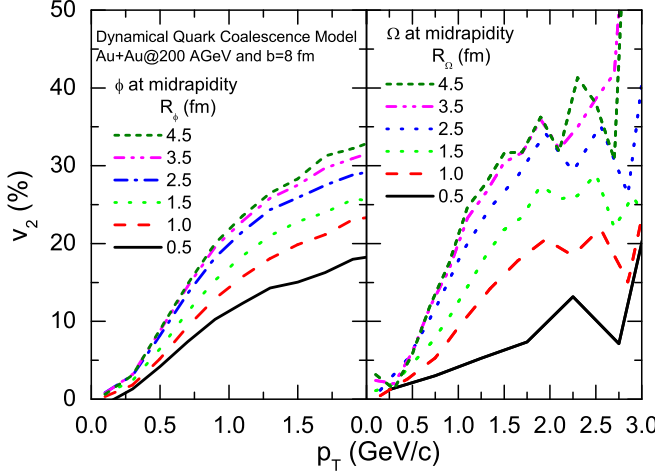


FIG. 13: (Color online)  $p_T$ -dependence of  $v_2$  of mid-rapidity  $\phi$  mesons (left panel) and  $\Omega$  baryons (right panel) in Au+Au collisions at  $\sqrt{s_{NN}} = 200$  GeV and  $b = 8$  fm with different values of the root-mean-square radii  $R_\phi$  and  $R_\Omega$ .

We first show in left panel of Fig. 13 the  $p_T$ -dependence of  $v_2$  for mid-rapidity  $\phi$  mesons in Au+Au collisions at  $\sqrt{s_{NN}} = 200$  GeV and  $b = 8$  fm for different values of the root-mean-square radius  $R_\phi$ . It is clearly seen that the  $v_2$  of  $\phi$  mesons depends strongly on the  $\phi$  meson size. It becomes larger with increasing  $R_\phi$  but changes little when  $R_\phi > 4.5$  fm. Similarly, we show in right panel of Fig. 13 the  $p_T$ -dependence of  $v_2$  for mid-rapidity  $\Omega$  baryons produced in the same collision with different values of  $R_\Omega$ . Similar to that of  $\phi$  mesons, the  $v_2$  of  $\Omega$  baryons also increases with increasing size of the  $\Omega$  baryon and saturates when  $R_\Omega > 4.5$  fm. The saturation of  $\phi$  meson and  $\Omega$  baryon  $v_2$  at large sizes observed in Fig. 13 is essentially due to the fact that the dynamical quark coalescence model approaches the naive momentum-space quark coalescence model, i.e., only partons with same momentum can coalesce into hadrons, when the hadron size is large enough. This can be easily seen from Eqs. (6) and (10) as the quark Wigner phase-space function becomes essentially delta functions in the relative momenta of coalescing partons when hadron sizes (i.e., the parameters  $\sigma_\phi$  and  $\sigma_\Omega$ ) are very large. As a result, we expect the valence-quark-number-scaled  $v_2$  of  $\phi$  mesons and  $\Omega$  baryons approaches the  $v_2$  of coalescing strange and antistrange quarks as their sizes increase. This is shown in Fig. 14 where it is seen that the  $p_T/n_q$ -dependence of  $v_2$  per valence quark or anti-quark  $n_q$  of mid-rapidity  $\phi$  mesons and  $\Omega$  baryons produced in Au+Au collisions at  $\sqrt{s_{NN}} = 200$  GeV and  $b = 8$  fm with  $R_\phi = R_\Omega = 4.5$  fm are indeed similar to the elliptic flow of mid-rapidity strange and antistrange

quarks ( $s + \bar{s}$ ) at freeze-out.

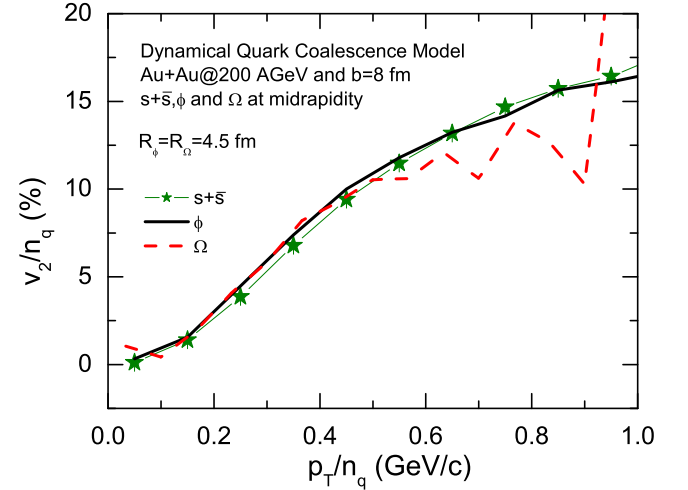


FIG. 14: (Color online) Same as Fig. 11 but with  $R_\phi = R_\Omega = 4.5$  fm.

## C. Fourth-order flow of $\phi$ and $\Omega$

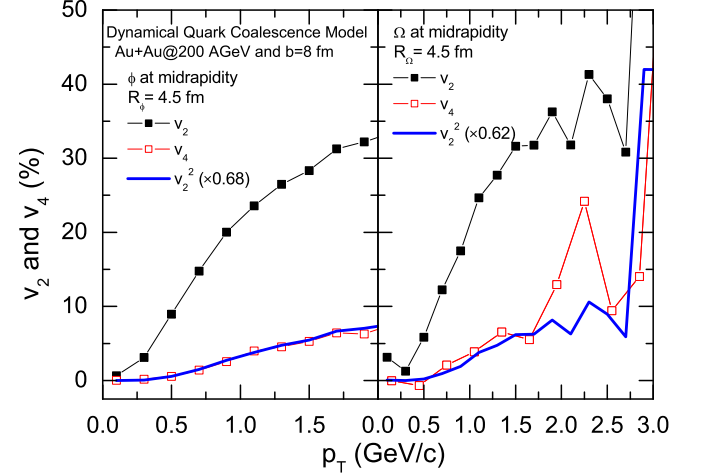


FIG. 15: (Color online) Same as Fig. 10 but with  $R_\phi = R_\Omega = 4.5$  fm.

For the scaling relation  $v_4(p_T) \sim v_2^2(p_T)$  among hadron anisotropic flows, as discussed above and in Refs. [27, 28], the dynamical quark coalescence model leads to a deviation of the scaling coefficient from that of the naive momentum-space quark coalescence model as a result of finite hadron sizes and nonzero parton relative momenta inside hadrons. The deviation is expected to disappear for large enough hadron sizes when the dynamical quark coalescence model approaches the

naive momentum-space quark coalescence model. This is demonstrated in Fig. 15 where we show the  $p_T$ -dependence of the anisotropic flows  $v_2$  (solid squares) and  $v_4$  (open squares) of mid-rapidity  $\phi$  mesons (left panel) and  $\Omega$  baryons (right panel) produced in Au+Au collisions at  $\sqrt{s_{NN}} = 200$  GeV and  $b = 8$  fm with large hadron sizes, i.e.,  $R_\phi = R_\Omega = 4.5$  fm. Also shown in Fig. 15 are  $0.68v_2^2$  (solid line in left panel) and  $0.62v_2^2$  (solid line in right panel). It is seen that the scaling coefficients of  $\phi$  mesons and  $\Omega$  baryons for such large hadron sizes indeed approach the values expected from the naive momentum-space quark coalescence model, i.e., about 0.68 for  $\phi$  mesons and 0.62 for  $\Omega$  baryons. We note that a larger hadron size generally gives a smaller scaling coefficient in the dynamical quark coalescence model.

## VI. QUARK MASS DEPENDENCE OF $\phi$ AND $\Omega$ TRANSVERSE MOMENTUM SPECTRA AND ANISOTROPIC FLOWS

In above calculations, we have used the current quark mass of 199 MeV for strange quarks, which is the default value in the AMPT model with string melting scenario. Usually, the constituent quark mass (about 500 MeV for the strange quark) is used in the quark coalescence model and the binding energy effect is thus small. In the following, we study the strange quark mass dependence of  $\phi$  meson and  $\Omega$  baryon production and their anisotropic flows by using a strange quark mass of 500 MeV but same strange quark space-time coordinates and momenta at freeze out as before. The quark mass effect thus shows up through the Lorentz transformation that changes the strange quark space-time coordinates and momenta in the rest frame of the  $\phi$  meson and  $\Omega$  baryon and thus affects their overlap with the quark Wigner phase-space functions inside hadrons.

### A. Yields and transverse momentum spectra of $\phi$ and $\Omega$

Using a strange quark mass of 500 MeV, we find that the yields of  $\phi$  mesons and  $\Omega$  baryons are both enhanced significantly compared to previous results with a strange quark mass of 199 MeV. For Au+Au collisions at  $\sqrt{s_{NN}} = 200$  GeV and  $b = 0$  (8) fm, the  $dN/dy$  at mid-rapidity for  $\phi$  mesons with  $R_\phi = 0.65$  fm changes from 8.0 (3.3) to 12.2 (4.8) while that with  $R_\phi = 0.47$  fm changes from 4.7 (2.0) to 7.3 (3.0) when the strange quark mass changes from 199 MeV to 500 MeV. To keep the  $dN/dy$  of  $\phi$  mesons at mid-rapidity unchanged requires a reduction of the  $\phi$  meson size from  $R_\phi = 0.65$  fm to 0.5 fm or from  $R_\phi = 0.47$  fm to 0.35 fm when the strange quark mass is increased to 500 MeV. For  $\Omega$  baryons, the value of  $dN/dy$  at mid-rapidity for  $b = 0$  (8) fm with  $R_\Omega = 1.2$  fm changes from 0.65 (0.26) to 1.36 (0.49) when the strange quark mass changes from 199

MeV to 500 MeV. A somewhat smaller  $\Omega$  baryon size of  $R_\Omega = 0.9$  fm is then needed to keep  $dN/dy$  of  $\Omega$  baryons at mid-rapidity unchanged when the strange quark mass is increased to 500 MeV.

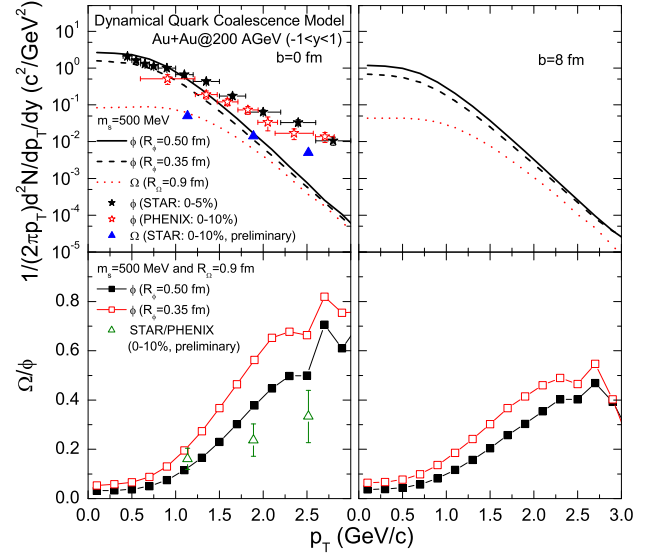


FIG. 16: (Color online) Same as Fig. 8 but with  $m_s = 500$  MeV and  $R_\phi = 0.5$  fm or 0.35 fm and  $R_\Omega = 0.9$  fm.

We also find that the larger strange quark mass of 500 MeV leads to a slightly stiffer transverse momentum spectra for  $\phi$  mesons and  $\Omega$  baryons. For  $R_\phi = 0.65$  (0.47) fm, the mean transverse momentum  $\langle p_T \rangle$  for the  $\phi$  meson changes from about 0.72 (0.73) and 0.68 (0.70) GeV/c for  $b = 0$  fm and  $b = 8$  fm, respectively, to about 0.74 (0.76) and 0.69 (0.72) GeV/c for  $b = 0$  fm and  $b = 8$  fm, respectively, when the strange quark mass changes from 199 MeV to 500 MeV. For  $\Omega$  baryons, the value of  $\langle p_T \rangle$  with  $R_\Omega = 1.2$  fm changes from about 0.93 and 0.83 GeV/c for  $b = 0$  fm and  $b = 8$  fm, respectively, to about 0.96 and 0.85 GeV/c for  $b = 0$  fm and  $b = 8$  fm, respectively, when the strange quark mass changes from 199 MeV to 500 MeV.

With the new parameters  $m_s = 500$  MeV,  $R_\phi = 0.5$  fm or 0.35 fm, and  $R_\Omega = 0.9$  fm fixed from the measured yields of  $\phi$  mesons and  $\Omega$  baryons, the transverse momentum spectra of midrapidity  $\phi$  mesons and  $\Omega$  baryons and their ratio in the same collision are shown in Fig. 16. As in Fig. 8, the corresponding data are also included in left panels of Fig. 16. For  $R_\phi = 0.5$  (0.35) fm and  $m_s = 500$  MeV, the mean  $\phi$  meson transverse momentum  $\langle p_T \rangle$  calculated from the  $\phi$  meson transverse momentum spectrum is about 0.76 (0.77) and 0.72 (0.74) GeV/c for  $b = 0$  fm and  $b = 8$  fm, respectively, which are still somewhat smaller than the experimental value of about 0.85-1.1 GeV/c [37, 38]. For  $\Omega$  baryons with  $R_\Omega = 0.9$  fm, their mean transverse momentum  $\langle p_T \rangle$  is about 1.05 and 0.94 GeV/c for  $b = 0$  fm and  $b = 8$  fm, respectively.

The  $\Omega/\phi$  ratio obtained from above new parameters is shown in lower panels of Fig. 16. Compared with the case of  $m_s = 199$  MeV, the  $\Omega/\phi$  ratio increases even more from low  $p_T$  to intermediate  $p_T$  of about 2.5 GeV/c, leading to a larger enhancement factor about 14 and 9 for  $b = 0$  fm and  $b = 8$  fm, respectively. The  $\bar{\Omega}^+/\phi$  at  $p_T \approx 2.5$  GeV/c is now about 0.30 and 0.22 for  $b = 0$  fm and  $b = 8$  fm, respectively, which are still significantly smaller than that of anti-protons to pions observed in experiments but remain comparable to the measured  $\Omega/\phi$  ratio for the larger  $\phi$  meson size of  $R_\phi = 0.5$  fm.

### B. Anisotropic flows of $\phi$ and $\Omega$

Using the fitted hadron size parameters for  $m_s = 500$  MeV, i.e.,  $R_\phi = 0.5$  fm or 0.35 fm and  $R_\Omega = 0.9$  fm, we show in left panel of Fig. 17 the  $p_T$  dependence of the anisotropic flows  $v_2$  (solid squares for  $R_\phi = 0.5$  fm and triangles for  $R_\phi = 0.35$  fm) and  $v_4$  (open squares for  $R_\phi = 0.5$  fm and triangles for  $R_\phi = 0.35$  fm) of mid-rapidity  $\phi$  mesons produced in Au+Au collisions at  $\sqrt{s_{NN}} = 200$  GeV and  $b = 8$  fm. Also shown in left panel of Fig. 17 are  $1.0v_2^2$  (solid line for  $R_\phi = 0.5$  fm) and  $1.1v_2^2$  (dashed line for  $R_\phi = 0.35$  fm). Similar results for  $\Omega$  baryons are shown in right panel of Fig. 17. Compared to those shown in Fig. 10 with a strange quark mass of 199 MeV, the strange quark mass only influences slightly the hadron elliptic flows with the larger strange quark mass of  $m_s = 500$  MeV giving a slightly smaller  $v_2$  at lower  $p_T$  while a slightly larger  $v_2$  at higher  $p_T$ . Also, the anisotropic flows of  $\phi$  mesons and  $\Omega$  baryons from the dynamical quark coalescence model with the larger strange quark mass of  $m_s = 500$  MeV still satisfy the scaling relation  $v_4(p_T) \sim v_2^2(p_T)$  with similar scaling coefficients as those for the strange quark mass of 199 MeV.

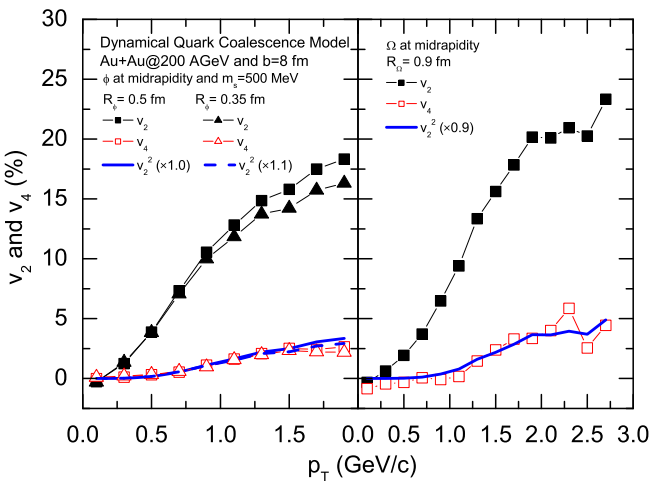


FIG. 17: (Color online) Same as Fig. 10 but with  $m_s = 500$  MeV and  $R_\phi = 0.5$  fm or 0.35 fm and  $R_\Omega = 0.9$  fm.

The  $p_T/n_q$ -dependence of  $v_2$  per valence quarks or anti-quarks for mid-rapidity  $\phi$  mesons and  $\Omega$  baryons produced in Au+Au collisions at  $\sqrt{s_{NN}} = 200$  GeV and  $b = 8$  fm, obtained with the large strange quark mass of 500 MeV,  $R_\phi = 0.5$  fm or 0.35 fm and  $R_\Omega = 0.9$  fm, is shown in Fig. 18 together with the elliptic flow of mid-rapidity strange and antistrange quarks ( $s + \bar{s}$ ) at freeze-out. It is seen that the  $v_2$  of mid-rapidity  $\phi$  mesons and  $\Omega$  baryons still satisfies approximately the valence number scaling in the dynamical quark coalescence model. However, the valence-quark-number-scaled  $v_2$  remains significantly smaller than the  $v_2$  of coalescing strange and antistrange quarks.

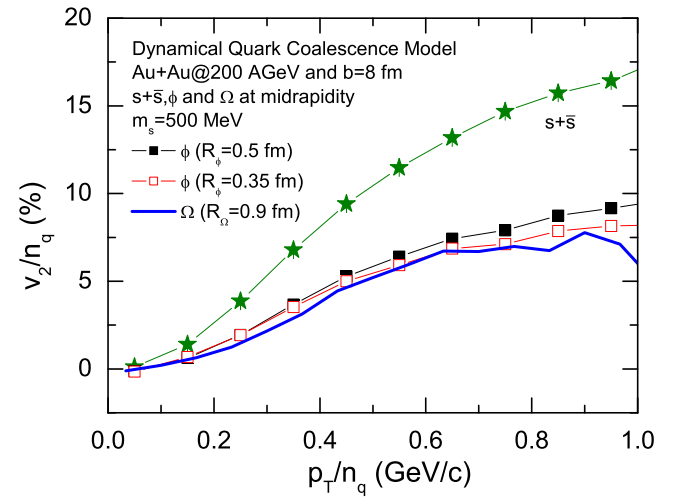


FIG. 18: (Color online) Same as Fig. 11 but with  $m_s = 500$  MeV and  $R_\phi = 0.5$  fm and 0.35 fm as well as  $R_\Omega = 0.9$  fm.

## VII. SUMMARY

Based on the parton phase-space information obtained from a multi-phase transport model within the string melting scenario, we have studied the production of  $\phi$  mesons and  $\Omega$  baryons and their anisotropic flows in Au+Au collisions at RHIC using a dynamical quark coalescence model, which requires information on the radii of  $\phi$  mesons and  $\Omega$  baryons. Fixing their radii by fitting measured yields of  $\phi$  mesons and  $\Omega$  baryons at mid-rapidity in central Au+Au collisions at  $\sqrt{s_{NN}} = 200$  GeV, we have evaluated their transverse momentum spectra in the same collision at impact parameter  $b = 0$  and 8 fm and also their anisotropic flows in the same collision at impact parameter  $b = 8$  fm. Comparing with its value at low transverse momenta, we have found that the ratio of the yield of  $\Omega$  baryons to that of  $\phi$  mesons is enhanced significantly at intermediate transverse momenta as observed in experiments.

We have further found that the elliptic flows of  $\phi$  mesons and  $\Omega$  baryons follow approximately the va-

lence quark number scaling. The valence-quark-number-scaled  $v_2$ 's of  $\phi$  mesons and  $\Omega$  baryons deviate, however, strongly from the underlying  $v_2$  of strange and antistrange quarks. Moreover, we have also studied the forth-order anisotropic flow  $v_4$  and found that the scaling relation of  $v_4(p_T) \sim v_2^2(p_T)$  observed experimentally for charged hadrons is satisfied by  $\phi$  mesons and  $\Omega$  baryons as well. It will be very interesting to compare these predictions with the experimental data that are being analyzed.

In addition, we have studied the dependence of above results on the radii of  $\phi$  mesons and  $\Omega$  baryons as well as the strange quark mass. Both the yields and anisotropic flows of  $\phi$  mesons and  $\Omega$  baryons are found to be sensitive to their radii. For sufficient large radii, the valence-quark-number-scaled  $v_2$ 's of  $\phi$  mesons and  $\Omega$  baryons approach the  $v_2$  of strange and antistrange quarks as in the naive momentum-space coalescence model. Also the scaling coefficient  $v_4(p_T)/v_2^2(p_T)$  is sensitive to hadron sizes. Although the strange quark mass was found to affect significantly the yields of  $\phi$  mesons and  $\Omega$  baryons, it does not change much their anisotropic flows. Our results thus suggest that in using the quark coalescence model to extract the parton dynamics in relativistic heavy ion collisions from hadron observables, it is important to take into account the quark structure of hadrons.

Although results from present study reproduces reasonably the observed transverse momentum dependence

of the  $\Omega/\phi$  ratio, the transverse momentum spectra of  $\phi$  mesons and  $\Omega$  baryons are too soft compared with measured ones. This has been attributed to the small current quark masses used in the AMPT model. Recent studies have shown that the equation of state of the QGP from the lattice QCD calculations can only be reproduced by partons with large masses [66, 67]. It is thus of great interest to improve the AMPT model by using massive partons and to study how the resulting parton dynamics affects the results obtained in present study. In addition, it is important to include in future studies the contribution from high momentum jets [68] as they are expected to affect the production of  $\phi$  mesons and  $\Omega$  baryons as well as their anisotropic flows at intermediate and high transverse momenta.

### Acknowledgments

We thank Professor Zong-Ye Zhang for helpful communications on the radius of the  $\Omega$  baryon in the quark model. This work was supported in part by the National Natural Science Foundation of China under Grant Nos. 10105008 and 10575071 (LWC) as well as by the US National Science Foundation under Grant No. PHY-0457265 and the Welch Foundation under Grant No. A-1358 (CMK).

---

[1] V. Greco, C.M. Ko, and P. Lévai, Phys. Rev. Lett. **90**, 202302 (2003); Phys. Rev. C **68**, 034904 (2003).  
[2] R.C. Hwa and C.B. Yang, Phys. Rev. C **67**, 034902 (2003); 064902 (2003).  
[3] R.J. Fries, B. Müller, C. Nonaka, and S.A. Bass, Phys. Rev. Lett. **90**, 202303 (2003); Phys. Rev. C **68**, 044902 (2003).  
[4] D. Molnar and S. A. Voloshin, Phys. Rev. Lett. **91**, 092301 (2003).  
[5] D. Molnar, J. Phys. G **31**, S421 (2005); *ibid.* **30**, S1239 (2004).  
[6] J. Ralfelski and B. Müller, Phys. Rev. Lett. **48**, 1066 (1982); Phys. Lett. **B101**, 111 (1982).  
[7] P. Koch, B. Müller and J. Ralfelski, Phys. Rep. **142**, 167 (1986); and the references therein.  
[8] J. H. Chen *et al.*, nucl-th/0504055.  
[9] J. Adams *et al.* [STAR Collaboration], Phys. Rev. Lett. **95**, 122301 (2005).  
[10] J.Y. Ollitrault, Phys. Rev. D **46**, 229 (1992).  
[11] H. Sorge, Phys. Lett. **B402**, 251 (1997); Phys. Rev. Lett. **78**, 2309 (1997);  
H. Sorge, Phys. Rev. Lett. **82**, 2048 (1999).  
[12] P. Danielewicz, R.A. Lacey, P.B. Gossiaux, C. Pinkenburg, P. Chung, J. M. Alexander, and R.L. McGrath, Phys. Rev. Lett. **81**, 2438 (1998).  
[13] Y. Zheng, C.M. Ko, B.A. Li, and B. Zhang, Phys. Rev. Lett. **83**, 2534 (1999).  
[14] P.F. Kolb, P. Huovinen, U. Heinz, and H. Heiselberg, Phys. Lett. **B500**, 232 (2001).  
[15] P. Huovinen, P.F. Kolb, U. Heinz, P.V. Ruuskanen, and S. Voloshin, Phys. Lett. **B503**, 58 (2001).  
[16] B. Zhang, M. Gyulassy, and C.M. Ko, Phys. Lett. **B455**, 45 (1999).  
[17] D. Molnar and M. Gyulassy, Nucl. Phys. **A698**, 379 (2002).  
[18] Z.W. Lin and C.M. Ko, Phys. Rev. C **65**, 034904 (2002).  
[19] M. Gyulassy, I. Vitev and X.N. Wang, Phys. Rev. Lett. **86**, 2537 (2001).  
[20] S.A. Voloshin, Nucl. Phys. **A715**, 379c (2003).  
[21] D. Teaney, J. Laureant, and E.V. Shuryak, Phys. Rev. Lett. **86**, 4783 (2001).  
[22] P.F. Kolb, J. Sollfrank, and U. Heinz, Phys. Lett. **B459**, 667 (1999).  
[23] D. Teaney and E.V. Shuryak, Phys. Rev. Lett. **83**, 4951 (1999).  
[24] P.F. Kolb, J. Sollfrank, and U. Heinz, Phys. Rev. C **62**, 054909 (2000).  
[25] P.F. Kolb, Phys. Rev. C **68**, 031902(R) (2003).  
[26] J. Adams *et al.* [STAR Collaboration], Phys. Rev. Lett. **92**, 062301 (2004).  
[27] L.W. Chen, C.M. Ko, and Z.W. Lin, Phys. Rev. C **69**, 031901(R) (2004).  
[28] P. Kolb, L.W. Chen, V. Greco, and C.M. Ko, Phys. Rev. C **69**, 051901(R) (2004).  
[29] A. Shor, Phys. Rev. Lett. **54**, 1122 (1985).  
[30] C.P. Singh, Phys. Rev. Lett. **56**, 1750 (1986).  
[31] H. van Hecke, H. Sorge and N. Xu, Phys. Rev. Lett. **81**, 5764 (1998).

- [32] S.A. Bass et al., Phys. Rev. C **60**, 021902 (1999); A. Dumitru, S.A. Bass, M. Bleicher, H. Stöcker, W. Greiner, Phys. Lett. **B460**, 411 (1999); S.A. Bass and A. Dumitru, Phys. Rev. C **60**, 064909 (2000).
- [33] Y. Cheng et al., Phys. Rev. C **68**, 034910 (2003).
- [34] S. F. Biagi et al., Nucl. Phys. **B186**, 1 (1981).
- [35] R. A. Muller, Phys. Lett. **B38**, 123 (1972).
- [36] J. Adams et al. (STAR Collaboration), Phys. Rev. Lett. **92**, 182301 (2004).
- [37] A. Adams et al. [SATR Collaboration], Phys. Lett. **B612**, 181 (2005).
- [38] S.S. Adler et al. [PHENIX Collaboration], Phys. Rev. C **72**, 014903 (2002); D. Mukhopadhyay et al. [PHENIX Collaboration], J. Phys. G **31**, S187 (2005).
- [39] C. Suire et al. [SATR Collaboration], Nucl. Phys. **A715**, 470c (2003).
- [40] Z.W. Lin, C.M. Ko, B.A. Li, B. Zhang, and S. Pal, Phys. Rev. C **72**, 064901 (2005).
- [41] X. N. Wang and M. Gyulassy, Phys. Rev. D **44**, 3501 (1991).
- [42] B. Zhang, Comput. Phys. Commun. **109**, 193 (1998).
- [43] T. Sjostrand, Comput. Phys. Commun. **82**, 74 (1994).
- [44] B. A. Li and C. M. Ko, Phys. Rev. C **52**, 2037 (1995); B.A. Li, A.T. Sustich, B. Zhang, and C.M. Ko, Int. Jour. Phys. E **10**, 267-352 (2001).
- [45] B. Zhang, C. M. Ko, B. A. Li, Z. W. Lin, and B. H. Sa, Phys. Rev. C **62**, 054905 (2000); B. Zhang, C. M. Ko, B. A. Li, Z. W. Lin, and S. Pal, *ibid.* **65**, 054909 (2002).
- [46] L.W. Chen and C.M. Ko, Phys. Lett. B, 2006, in press; nucl-th/0505044.
- [47] D. Kharzeev and M. Nardi, Phys. Lett. **B507**, 121 (2001).
- [48] Z. W. Lin, C. M. Ko, and S. Pal, Phys. Rev. Lett. **89**, 152301 (2002).
- [49] K.H. Ackermann et al. [STAR Collaboration], Phys. Rev. Lett. **86**, 402 (2001).
- [50] C. Adler et al. [STAR Collaboration], Phys. Rev. Lett. **87**, 082301 (2001).
- [51] F. Karsch, Nucl. Phys. **A698**, 199c (2002).
- [52] Z. Fodor, Nucl. Phys. **A715**, 319c (2003), and references therein; Z. Fodor and S.D. Katz, Phys. Lett. **B534**, 87 (2002).
- [53] J. Barrette et al. [E877 Collaboration], Phys. Rev. Lett. **73**, 2532 (1994).
- [54] H. Appelshauser et al. [NA49 Collaboration], Phys. Rev. Lett. **80**, 4136 (1998).
- [55] R. Mattiello et al., Phys. Rev. Lett. **74**, 2180 (1995); R. Mattiello et al., Phys. Rev. C **55**, 1443 (1997).
- [56] L.W. Chen, C.M. Ko, and B.A. Li, Phys. Rev. C **68**, 017601 (2003); Nucl. Phys. **A729**, 809 (2003).
- [57] L.W. Chen, V. Greco, C.M. Ko, S.H. Lee, and W. Liu, Phys. Lett. **B601**, 34 (2004).
- [58] A.T.M Aerts and C.B. Dover, Phys. Rev. D **28**, 450 (1983).
- [59] R. Scheibl and U. Heinz, Phys. Rev. C **59**, 1585 (1999).
- [60] L.W. Chen, V. Greco, C.M. Ko and F. Kolb, Phys. Lett. **B605**, 95 (2005).
- [61] S.S. Adler et al. [PHEHIX Collaboration], Phys. Rev. C **69**, 034909 (2004).
- [62] V. Greco and C. M. Ko, Phys. Rev. C **70**, 024901 (2004) [arXiv:nucl-th/0402020].
- [63] V. Greco and C. M. Ko, arXiv:nucl-th/0505061.
- [64] S. Pratt and S. Pal, Nucl. Phys. Rev. C **71**, 014905 (2005); Phys. A749, 268c (2005).
- [65] B. Muller, R. J. Fries and S. A. Bass, Phys. Lett. **B618**, 77 (2005) [arXiv:nucl-th/0503003].
- [66] P. Levai and U. W. Heinz, Phys. Rev. C **57**, 1879 (1998) [arXiv:hep-ph/9710463].
- [67] A. Peshier and W. Cassing, Phys. Rev. Lett. **94**, 172301 (2005) [arXiv:hep-ph/0502138].
- [68] V. Greco, C. M. Ko and I. Vitev, Phys. Rev. C **71**, 041901 (2005) [arXiv:nucl-th/0412043].